Dynamic Channel Modeling for Indoor Millimeter-Wave Propagation Channels Based on Measurements

Cai, Xuesong; Zhang, Guojin; Zhang, Chao; Fan, Wei; Li, Jinxing; Pedersen, Gert Frølund

Published in:
IEEE Transactions on Communications

DOI (link to publication from Publisher):
10.1109/TCOMM.2020.3001614

Publication date:
2020

Document Version
Accepted author manuscript, peer reviewed version

Dynamic Channel Modeling for Indoor Millimeter-Wave Propagation Channels Based on Measurements

Xuesong Cai, Guojin Zhang, Chao Zhang,
Wei Fan, *Senior Member, IEEE*, Jinxing Li and Gert Frølund Pedersen

***Abstract*—In this contribution, a recently conducted measurement campaign for indoor millimeter-wave propagation channels is introduced. A vector network analyzer (VNA)-based channel sounder was exploited to record the channel characteristics at the frequency band from 28-30 GHz. A virtual uniform circular array (UCA) with a radius of 0.25 m was formed using a rotator with 360 steps. Moreover, by taking advantage of fiber-optic technique applied in the channel sounder, measurements at 50 positions were performed from an indoor hall to an indoor corridor along a long pre-defined route. A low-complexity high-resolution propagation estimation (HRPE) algorithm is exploited to estimate the propagation parameters of multipath components (MPCs). Based on the HRPE estimation results, a novel clustering identification and tracking algorithm is proposed to trace clusters. Composite channel characteristics, cluster-level characteristics and dynamic (or birth-death) behaviours of the clusters are investigated, which constitute a dynamic model for the indoor millimeter-wave channel.**

***Index terms*—** Millimeter wave, cluster, dispersions, birth-death and dynamic channel.

I. Introduction

In recent years, an explosive growth of wireless communication data traffic is observed. In this context, millimeter wave (mm-wave) is expected to contribute high data-rate and large capacity for future fifth-generation (5G) communication system due to the large amount of available frequency spectrum [1], [2]. However, mm-wave transmission suffers severe attenuation caused by propagation loss and blockage compared to the sub-6 GHz bands. In order to meet the ever-increasing demands, enabling 5G technologies, e.g. massive multiple-input-multiple-output (MIMO), ultra-dense network, etc. [3]–[5], have been studied. Specially, beamforming with massive MIMO offers great promise as the high-gain beams can compensate the attenuation and also provide increased capacity to multiple users (so-called MU-MIMO) [6]. These technologies necessitate special strategies such as beam acquisition and tracking [7], making it a prerequisite to gain explicit knowledge of mm-wave channels (especially the dynamic behaviours) for performance evaluation of 5G techniques and communication systems.

Many research groups and organizations have made efforts to study and develop channel models in either theoretical or experimental manners for frequencies up to 100 GHz. In [8]–[11], ray-tracing simulation tools were exploited to investigate the mm-wave channels in outdoor and indoor scenarios. The authors in [12] applied the propagation graph theory to model 60 GHz channel power angular spectra in an office environment. Though inspiring results were provided by these numerical studies, the realistic scenarios which are far more complicated compared to simulated scenarios need to be characterized by conducting field measurements. According to the different measurement methodologies, we classify the measurement-based investigations into three categories with several examples discussed in each category. *i) Directional scan sounding (DSS):* Horn antennas are widely used in mm-wave channel measurements since they provide a significant level of directivity and gain. The horn antennas are usually installed on a rotational platform for capturing the signals from different directions. The total received power could be obtained by summing the received powers at each steering direction [13]. Large scale omnidirectional path loss models were developed based on this concept as presented in [14], [15] for both line-of-sight (LoS) and non-LoS (NLoS) scenarios. Furthermore, the measured channels at different steering directions construct the joint delay-angle-power spectra, e.g. as shown in [12], [16]. A double-directional MIMO channel model was presented to demonstrate the consistency between extracted clusters and geometry of the conference room at 60 GHz [17]. Note that in the DSS measurements the additional phase noise introduced by the rotation-center deviation and cable bending should be carefully considered or calibrated, especially in high frequency bands [18], [19]. *ii) Virtual antenna arrays (VAA):* Different from DSS method, VAA relies on a positioner to move an antenna to different locations so that a 2D or 3D array can be formed. For examples, channel characteristics in delay and spatial domain were investigated in [20]–[23] for mm-wave bands with uniform arrays. The authors in [24] established intracluster and intercluster angular spread models with Laplace distribution and Gaussian mixture distribution. Moreover, the behaviour of clusters evolving across a large antenna array was investigated in [25]. Note that in both DSS and VAA measurements, it takes time for the

The work was partially supported by Huawei technologies and InnoExplorer project (2019 9122-00089A) funded by Innovation Fund Denmark.

X. Cai, G. Zhang, C. Zhang, W. Fan and G. F. Pedersen are with the Department of Electronic Systems, Faculty of Engineering and Science, Aalborg University, Aalborg 9220, Denmark (e-mail: xuc@es.aau.dk; guojin@es.aau.dk; czhang@es.aau.dk; wfa@es.aau.dk; gfp@es.aau.dk).

J. Li is with Huawei Technologies, Shanghai Research Institute, Shanghai 201206, China (e-mail: lijinxing3@huawei.com).

rotator or positioner to scan the pre-set locations. Therefore, both approaches can be only applied in static environments. *iii) Real antenna arrays (RAA):* Apart from the above mentioned methods, using RAA is also an alternative. For examples, a channel sounder with antenna arrays up to 2×16 at mm-wave band and up to 16×128 at sub-6 GHz band using RAAs and switches was presented in [26]. In [27], [28], a very large RAA-based sounder with 160 dual-polarized antennas was developed and validated in LoS mobile channels, though the working frequency is below 6 GHz. RAA has the advantages in e.g. measuring channels in fast-moving scenarios. However, it requires a huge amount of resources, and the calibration and decoupling among antennas are difficult and critical especially at mm-wave bands. This is also the reason for the scarcity of RAA measurements in mm-wave bands.

Despite considerable efforts have been made in mm-wave propagation channel measurements and modeling, some important features are still inadequately considered in literature. The reasons are threefold. *i)* The measurement distance, i.e. the distance between transmitter (Tx) and receiver (Rx), is usually limited, e.g. in [29], [30], due to the high power attenuation in the coaxial-cable. These models may exhibit poor performance in scenarios like hall or airport where the distance between the users and base stations can be tens of meters. *ii)* Regarding the MPC parameter estimation, the coherent information across a whole large-array or the whole band is usually not adequately exploited. This is basically due to the missing of appropriate estimation algorithms or the prohibitively high computation-complexity. For examples in [17], [25] the authors decompose the very large arrays into several sub-arrays (and also the whole bands into several sub-bands) to make the plane-wave assumption valid so that the space-alternating-generalized-expectation-maximization (SAGE) algorithm can be applied. However, this in turns lower the accuracy and resolution. Similarly, the radiation pattern of the horn antenna used in the DSS measurements is usually hard to be de-embedded from the raw data. *iii)* Another main deficiency of the existing models is lack of consideration of the channel spatial consistency. In other words, the channel evolution behaviours when either Tx or Rx moves are not addressed in most of the investigations. However, the dynamic characteristics are crucial for system performance evaluation e.g. in terms of beam management especially for 5G and beyond systems where beamforming (based on massive MIMO) is considered the key technology. To support for beam operations in the performance evaluation under dynamic propagation scenarios, it is desirable that moving of Rx or Tx along a long route is enabled in the measurement campaign.

To address the above mentioned gaps, we carry out mm-wave channel measurements at 28-30 GHz frequency band using virtual uniform circular array (UCA) with both indoor hall and corridor scenarios considered. The main contributions and novelties of this paper are summarized as follows:

- By exploiting the fiber-optic technology in a vector network analyzer (VNA)-based channel sounder, a decently long-distance measurement campaign with closely spaced UCA positions was conducted in the indoor scenario. Moreover, the dynamic range was also enhanced due to the low signal-attenuation in the optic fiber. Totally 50 UCA positions were applied along a pre-defined route of around 48 m, which allows us to investigate the dynamic behaviors of the mm-wave channel.
- A complexity-efficient high resolution parameter estimation (HRPE) algorithm [31] is adopted for the ultra-wideband large-scale UCA. The coherent information across the large array and the whole frequency band can be adequatedly exploited by taking the spherical propagation into account. The accuracy and resolution of the estimated multipath-component (MPC) parameters are significantly enhanced.
- Based on the HRPE estimation results, a novel cluster identification and tracking algorithm is proposed to trace the dynamic clusters along the measurement route. Composite-level parameters, cluster-level parameters and dynamic parameters that characterize the "birth-death" behaviors of clusters are investigated. The established realistic dynamic channel model is essential for performance evaluation for 5G and beyond systems.

The rest of the paper is organized as follows. Sect. II elaborates the measurement scenarios and specifications in the measurement campaign. Sect. III presents some typical channels. In Sect. IV, data processing including the high-resolution propagation parameter estimation and cluster identification and tracking is elaborated. Based on Sect. IV, the established dynamic channel model is investigated in Sect. V. Finally, conclusive remarks are included in Sect. VI.

II. Measurement campaign

In this section, a recently conducted measurement campaign in an indoor area with a hall and a corridor is presented. The measurement scenarios and measurement equipment are introduced in Sect. II-A. The measurement configuration that includes the Tx and Rx antennas, frequency band, array configuration etc. is elaborated in Sect.II-B.

A. Measurement environment and channel sounder

The measurement campaign was conducted in an indoor environment. Fig. 1(a) illustrates its top-view geometry. As illustrated in Fig. 1(a), the indoor area has an irregularly-shaped hall and a connecting corridor. The dimension of the hall is approximately $44\times25\times10\,\mathrm{m}^3$ (length$\times$width$\times$height). Fig. 1(b) illustrates a photo taken in the hall. It can be observed that the hall is characterized by stairs, tables, metal supporting pillars (yellow circles), concrete supporting pillars (white circles) and walls. The connecting corridor is around 3.6 m wide and 33 m long. As illustrated in Fig. 1(c), the corridor has a concrete wall on one side and a glass wall on the other side. A vector network analyzer (VNA) and fiber-optic based channel sounder was used in the measurement. The VNA was exploited to excite the channel and record the channel transfer functions (CTFs), and the fiber optic cable was employed for prolonging the measurement distance (Tx-Rx distance) by

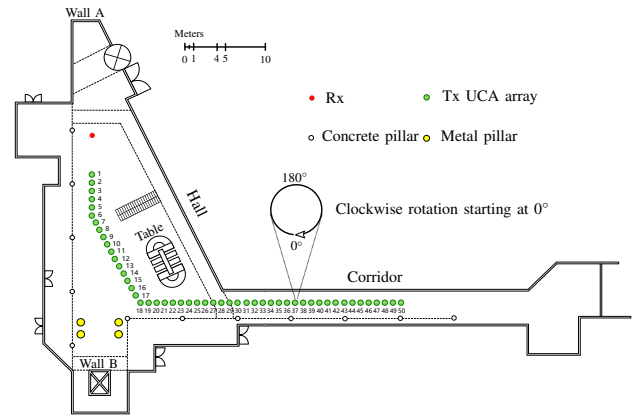

(a)

(b)

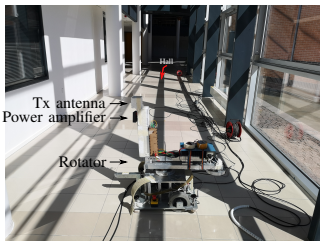

(c)

Fig. 1: The indoor hall and corridor where the measurement campaign was conducted. (a) The top-view sketch of the indoor area with measurement points marked. (b) A photo taken in the indoor hall. (c) A photo taken in the indoor corridor.

taking advantage of its low attenuation to signals in the cable. It has been demonstrated in [32] that a maximum dynamic range of 112 dB can be obtained at 30 GHz using a fiber-optic cable of length 300 m.[1] Furthermore, a phase compensation scheme was applied using photo detector, optic power splitter, optic circulator, etc. to calibrating the phase changes in the optic cable caused by e.g. thermal and mechanical stress. Readers are referred to [32], [33] for the detailed design of the measurement system. The model numbers of the different components used in the channel sounder can be found in Table I in [32]. The performance of the channel sounder has also been validated in [32], [33].

B. Measurement setup

During the measurement, an omni-directional biconical antenna (A-INFO-SZ-2003000/P [34]) was exploited in the Rx side and fixed at the location indicated by the red dot in Fig. 1(a). As illustrated in Fig. 1(b), the height (above ground) of Rx was set as 3 m. At the Tx side, another omni-directional biconical antenna [35] was placed on the rotator with a height (above ground) of 1.15 m as illustrated in Figs. 1(b) and 1(c). The Tx was moving in the indoor area from position to position as indicated by the green dots in Fig 1(a). Therefore, it is possible to regard the Rx and Tx as a base-station and a mobile user, respectively. Totally $K = 50$ different positions were performed along a predefined route. The distance of the whole route was 43.5 m, and the distances between neighboring positions were 0.9 m, 0.85 m and 0.9 m for positions 1 to 6, 6 to 18 and 18 to 50, respectively. At each position, a virtual UCA was formed by rotating the Tx antenna clockwise along a circle. The radius r, steps number M and starting point were kept the same for all the 50 positions. As shown in the zoomed-in sketch in Fig. 1(a) for position 36, the radius was $r = 0.25$ m, the number of steps to complete the circle was $M = 360$, and the starting point (i.e. the first UCA element) was at 0°. The distance between neighboring UCA elements was 4.4 mm which is smaller than the half wavelength at 30 GHz, so that the angular aliasing can be avoided [36]. The frequency range in the VNA was set from 28 GHz to 30 GHz with 2000 sweeping points. The intermediate bandwidth and average factor were set as 1 kHz and 1, respectively. It took 1.844 s to sweep 2000 frequency points for one UCA element. With guard time needed to move the antenna mechanically, the time gap between two sweeps was set as 3 s. Note that a back-to-back calibration for the channel sounder was performed before the formal measurements to remove the system response. It can be calculated that the frequency step was around 1 MHz which corresponds to a propagation distance window with length of 300 m. It was appropriately set to capture all paths with far propagation distances in the indoor environment.[2] Table I and Table II summarize the measurement specifications and antenna specifications applied in the measurement, respectively.

Table I: Measurement specifications applied in the measurement campaign.

Measurement specifications			
Tx UCA height (above ground)	1.15 m	Rx height (above ground)	3 m
UCA array radius	0.25 m	Frequency range	28-30 GHz
UCA elements number	360	Frequency points	2000

Table II: Specifications of Tx and Rx antennas applied in the measurement campaign.

Antenna specifications		
Antenna	Rx Biconical [33]	Tx Biconical [34]
Operating frequency range	2-30 GHz	1.5-41 GHz
Typical gain	6 dBi@29 GHz	4.5 dBi@29 GHz
Azimuth pattern	Omni	Omni
Polarization	Vertical	Vertical

III. Channel Characterization

As elaborated in Sect. II-B, at each Tx position 360 CTFs $H(m, f)$ were recorded where m and f represent the step index and frequency, respectively. By applying the inverse discrete Fourier transform (IDFT) to $H(m, f)$ with respect to f, 360 channel impulse responses (CIRs) $h(m, \tau)$ for the array can be obtained. We denote the 360 CIRs for a

[1]The channel sounder was designed with maximum Tx-Rx distance as 300 m to also cope with, e.g., outdoor measurements. Considering the fiber-optic cable has very low attenuation (which is less than 1 dB/km at 30 GHz [32]), the long cable was kept for the indoor scenarios, although the Tx-Rx distance was less than 300 m.

[2]It is worth noting that by applying the measurement configuration, all paths with power above the noise floor can be appropriately captured since no delay aliasing was observed, and the noise floor observed in the channel impulse response was around -140 dB. The dynamic ranges of the color-bars in Figs. 2 and 3 are confined referring to the maximum power just for illustration purpose.

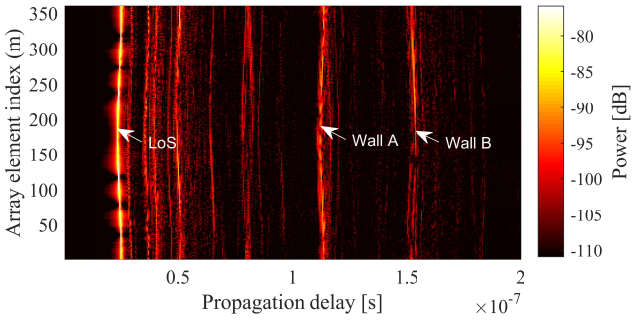

(a)

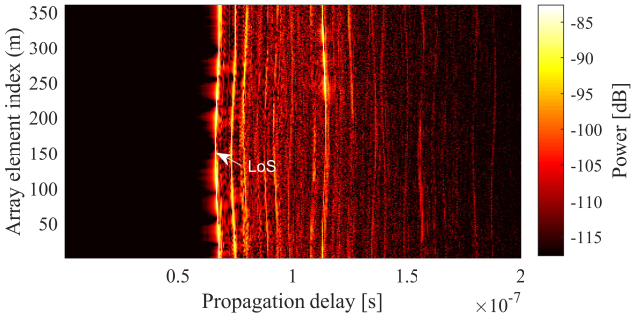

(b)

Fig. 2: Example CCIRs obtained in the hall. (a) Position 1. (b) Position 18.

position as concatenated CIRs (CCIRs). In this section, some typical measured CCIRs are presented, and the underlying propagation mechanisms are discussed.

i) CCIRs in hall scenario: Figs. 2(a) and 2(b) illustrate the CCIRs, i.e. $|h(m,\tau)|^2$, for positions 1 and 18 respectively in the hall. It can be observed that multiple curves exist in the figures. This is due to the 2 GHz bandwidth, i.e., a delay resolution of 0.5 ns or a distance resolution of 0.15 m. That is, the delay variation of a propagation path across the array aperture with radius of 0.25 m can present as a curve in a CCIRs figure. At position 1 as illustrated in Fig. 2(a), it can be clearly observed that the shape of the LoS path is a "("-alike curve. This is consistent with the fact that the delay of LoS path at the 180th array element is minimum for position 1. This also indicates the fact that the shape of a curve can reflect the angle information of a path to a certain extent. For example, as indicated by the arrow with text "Wall A" in Fig. 2(a), a curve with a similar shape to that of the LoS path can be observed. By checking its propagation delay, it can be inferred that this curve is contributed by "Wall A" as indicated in Fig. 1(a).[3] Moreover, the curve attributed to "Wall B" as indicated in Fig. 1(a) is also marked in Fig. 2(a). It can be observed that its shape is opposite to that of the LoS path and the "Wall A" curve. Furthermore, we can observe some other curves with different shape orientations.[4] They are

[3]The signal interacted with "Wall A" but not necessarily only with "Wall A".

[4]Orientation herein can be interpreted as the index of the element with minimum delay in a curve.

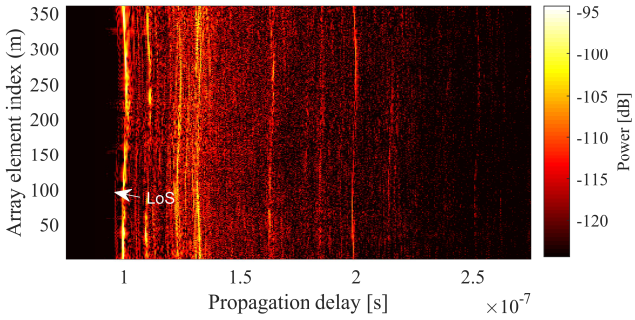

Fig. 3: An example CCIRs obtained at position 31 in the corridor.

contributed by the pillars, side walls, etc. in the hall. Different from the "clean" LoS trajectory, it can be observed that these NLoS curves may blur in the CCIRs figure. This indicates that multiple paths can occur with similar delays and angles, e.g. possibly caused by the scattering effects at pillars and walls. Fig. 2(b) illustrates the CCIRs figure at position 18. It can be observed that the index of the array element with minimum delay in the LoS curve shifts to a value smaller than 180, which demonstrates that the LoS path angle is less than 180°. This is consistent with the geometry between Tx and Rx at this position. Moreover, due to the distance between Tx and Rx becomes larger, the channel power also decreases. *ii) CCIRs in corridor scenario:* Fig. 3 illustrates an example CCIRs at position 31 in the corridor. Since the hall wall and corridor wall lie in between the Rx and Tx at this position as shown in Fig. 1(a), it can be observed from Fig. 3 that the LoS path is blocked. The channel power also decreases more.

IV. Data Processing

By examining the CCIRs figures in Figs. 2 and 3, it can be observed that the channel experiences obvious changes from the hall to the corridor in delay, angle and power domains. To gain more insights into how the channel evolves in the indoor area, high-resolution information of the channel is required. In this section, a HRPE algorithm is exploited to obtain the high-resolution propagation parameters, i.e. delays, azimuth angles, complex amplitudes, etc. of MPCs from the measured CTFs $H(m,f)$, which is discussed in Sect. IV-A. Based on the HRPE estimation results, a multipath-component-distance (MCD) threshold-based cluster identification and tracking algorithm is proposed in Sect. IV-B to track the dynamic behaviours of the channel.

A. High-resolution MPC parameter estimation

As elaborated in Sect. II-B, the UCA radius r was set as 0.25 m. The large aperture is advantageous to obtain a high angle-resolution [36]. Meanwhile, the Fraunhofer distance [37, Ch. 2.2.3], i.e. $\frac{8r^2}{\lambda}$, for the UCA is calculated as 50 m at 30 GHz where λ denotes the wavelength. This means that in the indoor environment, the spherical propagation is non-negligible since plane wave assumption can only be considered valid when the distance from a spherical-wavefront center to an array is much larger than the Fraunhofer distance.

Therefore, to gain accurate high-resolution estimation results, spherical propagation must be considered in the propagation parameter estimation to avoid model mismatch [38]. The underlying signal model for the channel impulse response can be formatted as

$$h(\tau,\phi,\theta,d)=\sum_{\ell=1}^{L}\alpha_\ell\delta(\tau-\tau_\ell)\delta(\phi-\phi_\ell)\delta(\theta-\theta_\ell)\delta(d-d_\ell), \tag{1}$$

and considering the UCA configuration, the measured array CTFs $H(m,f)$ can be written as [31]

$$H(m,f)=\sum_{\ell=1}^{L}\frac{d_\ell}{d_{\ell,m}}\alpha_\ell e^{-j2\pi f(\tau_\ell+\frac{d_{\ell,m}-d_\ell}{c})}+n(m,f) \tag{2}$$

with

$$d_{\ell,m}=\sqrt{{d_\ell}^2+r^2-2rd_\ell\cos\theta_\ell\cos\left(\phi_\ell-\frac{2\pi(m-1)}{M}\right)} \tag{3}$$

where L denotes the total number of MPCs, α_ℓ, τ_ℓ, θ_ℓ and ϕ_ℓ represent respectively the complex amplitude, propagation delay, elevation angle and azimuth angle of the ℓth path with UCA center as the reference point, d_ℓ denotes the distance from the UCA center to the spherical-wavefront center, $d_{\ell,m}$ indicates the distance from the mth array element to the spherical-wavefront center, c is the light speed, and $n(m,f)$ denotes the complex Gaussian noise. The parameters to be estimated for all the 50 positions are $\boldsymbol{\Theta}=[\boldsymbol{\Theta}^{(1)},\ldots,\boldsymbol{\Theta}^{(K)}]$ where $\boldsymbol{\Theta}^{(k)}=[\alpha_\ell^{(k)},\tau_\ell^{(k)},\theta_\ell^{(k)},\phi_\ell^{(k)},d_\ell^{(k)};\ell=1,\ldots,L^{(k)}]$, and k is inserted for the reason that the path number at a different position can be different.

Since the so-called narrowband assumption in array signal processing [36] is not valid due to the 2 GHz bandwidth and the large array aperture, i.e., the array aperture is much larger than the inverse bandwidth multiplied by the light speed, the widely used Space-Alternating Generalized Expectation-Maximization (SAGE) algorithm [17], [25], [39] is not applicable in our case. The complexity of the Expectation-Maximization (EM) algorithm [40], [41] is prohibitively high due to the multiple-dimensional joint-parameter-searching. We hence exploit a low-complexity HRPE estimator [31] to estimate $\boldsymbol{\Theta}$. The basic procedure mainly includes three steps. *i)* Firstly, obtain the high-resolution delay-element trajectories by applying a HRPE principle (e.g SAGE) only in delay domain for all the M UCA elements individually. *ii)* Secondly, locate a path trajectory across the array. This is achieved by exploiting a beamformer proposed in [42] to obtain roughly the delay and azimuth of this path trajectory. *iii)* Finally, retrieve the array transfer functions for this path according to the identified path trajectory. Then perform low-complexity parameter searching for the retrieved array responses, and update the original $H(m,f)$ by removing this path from it. Repeat steps *ii)* and *iii)* until the channel power is adequately extracted. Readers are referred to [31] for the detailed principle of the HRPE algorithm. A similar low-complexity HRPE algorithm generalized for an arbitrary array geometry can also be found in [43]. In practice, total path number is set adequately large to fully extract the channel power above the noise floor in step *i)* of the HRPE algorithm, and the valid MPCs number $L^{(k)}$ can be automatically determined in step *ii)* of the HRPE algorithm [31]. Fig. 4 illustrates an example estimated delay-azimuth-power spectrum at position 1 in the hall with its CCIRs illustrated in Fig. 2(a). It can be observed more obviously in Fig. 4 that the azimuths for LoS path and "Wall A" curves are near to 180°, and the azimuth for "Wall B" curves are near to 360° (or 0°). This demonstrates that the HRPE algorithm performs well to extract the high-resolution channel information. Moreover, it can be observed that MPCs are distributed in different groups. As conventionally termed in literature, we denote a group of MPCs with similar delays and angles as a cluster. In the sequel, cluster identification and tracking are elaborated.

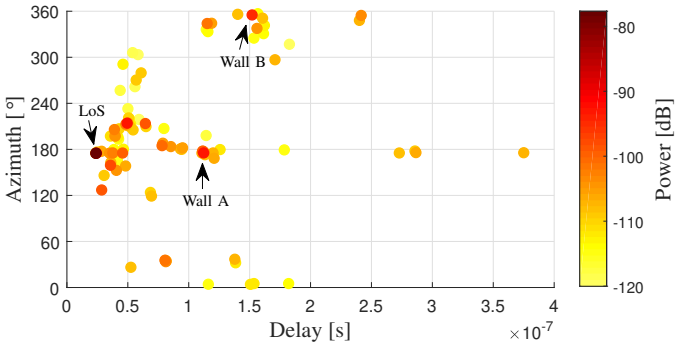

Fig. 4: An example high-resolution delay-azimuth-power spectrum estimated using the HRPE algorithm at position 1 in the hall.

B. Cluster identification and tracking

Several algorithms have been proposed to identify and/or track clusters in joint power-delay-angular domain. In [44], an algorithm combines K-Power-Means (KPM) and Kalman filter was proposed. KPM considers power in the MCD calculation and is a variant of KMeans [45]. The performances of KPM and KMeans are highly dependent on the initialization of clusters number and centroids. In [46], a Kernel-Power-Density algorithm was proposed by assuming Gaussian kernel-density in delay domain and Laplacian kernel-density in angular domain, respectively. A Gaussian-mixture-model (GMM) based method was exploited in [18] by assuming the cluster data obey multivariate Gaussian distribution. Recently, a MCD-threshold based principle was proposed in [17]. The investigations in [18], [47] show that the threshold principle outperforms GMM, KPM and KMeans, since the optimum threshold is physically linked to the cluster size/distribution [47], and any prior assumptions of clusters in terms of number, shapes, distributions, etc. are not required. Therefore, the proposed cluster identification and tracking algorithm in this section is based on the MCD-threshold principle.

The MPC distance (MCD) was firstly introduced in [48] to quantify the multipath separation where the MPC parameters present in different units and orders of magnitude. It was then demonstrated in [49] that the clustering performance improves

considerably with MCD as distance measures compared to that with squared Euclidean distance measures. In angular domain, the MCD between MPCs i and j is obtained as

$$\mathrm{MCD}_{\mathrm{Tx/Rx},ij} = \frac{1}{2}\left| \begin{pmatrix} \sin\theta_i \cos\phi_i \\ \sin\theta_i \sin\phi_i \\ \cos\theta_i \end{pmatrix} - \begin{pmatrix} \sin\theta_j \cos\phi_j \\ \sin\theta_j \sin\phi_j \\ \cos\theta_j \end{pmatrix} \right| \quad (4)$$

for Tx side and Rx side separately. In delay domain, the MCD is calculated as

$$\mathrm{MCD}_{\tau,ij} = \zeta \cdot \frac{|\tau_i - \tau_j|}{\Delta\tau_{\max}} \cdot \frac{\tau_{\mathrm{std}}}{\tau_{\max}} \quad (5)$$

where $\Delta\tau_{\max} = \max_{i,j}\{|\tau_i - \tau_j|\}$ for all pairs of (i,j), τ_{std} denotes the standard deviation of the delays, and ζ indicates an appropriate delay scaling factor that gives delay more "importance" when necessary which has advantageous effects when clustering real-world data [49]. The resulting MCD between two MPCs is then obtained as

$$\mathrm{MCD}_{ij} = \sqrt{\|\mathrm{MCD}_{\mathrm{Tx},ij}\|^2 + \|\mathrm{MCD}_{\mathrm{Rx},ij}\|^2 + \mathrm{MCD}_{\tau,ij}^2} \quad (6)$$

Note that for the channels observed in our case, $\|\mathrm{MCD}_{\mathrm{Rx},ij}\|^2$ in (6) is omitted since we only obtained the angular information at the UCA array side. Moreover, due to the low elevation resolution offered by the the 2D UCA, we also omit θ in the calculation of (4). For a cluster grouped by MPCs whose path indices are in set $\mathcal{S}_c$, its cluster centroid is calculated as

$$\mu_c = \frac{\sum_{\ell\in\mathcal{L}_c} |\alpha_\ell|^2 \cdot [\tau_\ell, \phi_\ell]^T}{\sum_{\ell\in\mathcal{L}_c} |\alpha_\ell|^2} \quad (7)$$

where T indicates transpose operation.

The proposed algorithm includes two parts. The first part is to identify clusters for all the K positions individually, and the second part is to track clusters between neighboring positions. The proposed cluster identification algorithm of the first part is elaborated in Algorithm 1. It is an improved variant of the algorithms reported in [17], [47]. The basic principle is to firstly initialize clusters by iteratively assigning MPCs adequately near to the current reference point which is chosen as the MPC with highest power among the remaining MPCs. The term "adequately near to" means that the MCD of a path to the reference path is lower than a pre-defined MCD threshold $\eta_{\mathrm{MCD},1}$. Then the overall intra-cluster MCDs are minimized by exploiting the previous cluster centroids as new reference points and updating the cluster centroids iteratively. The selection of the threshold $\eta_{\mathrm{MCD},1}$ is crucial. We exploit several cluster validity indices (CVIs) to choose a suitable value. The CVIs [47], [50]–[52] include Davies-Bouldin index, Calinski Harabasz index, generalized Dunn index, Xie and Beni index, Pakhira-Bandyopadhyay-Maulik index and SV index. Basically, these indices evaluate the compactness inside clusters and separativeness among clusters. As suggested in [51], the score fusion of all the CVIs is exploited as

$$\mathrm{SF}_{\mathrm{g}} = \left(\prod_{i=1}^{I} v_i\right)^{1/I} \quad (8)$$

where v_i denotes the normalized score for the ith CVI, and I represents the number of CVIs. Note that for the CVI whose optimal solution is obtained at smallest value (e.g. the XB index), it was modified as $(1 - v_i)$ before inserted into (8) so that the optimal solution is obtained at the largest SF_{g} value. Fig. 5 illustrates the SF_{g} variation (normalized to the largest value) versus $\eta_{\mathrm{MCD},1}$ variation for position 1. It can be observed that the largest SF_{g} value is obtained at $\eta_{\mathrm{MCD},1}$ equals 0.37 which is hence selected as the optimal threshold in the proposed clustering algorithm for position 1. The thresholds for the other positions are obtained with the same approach.

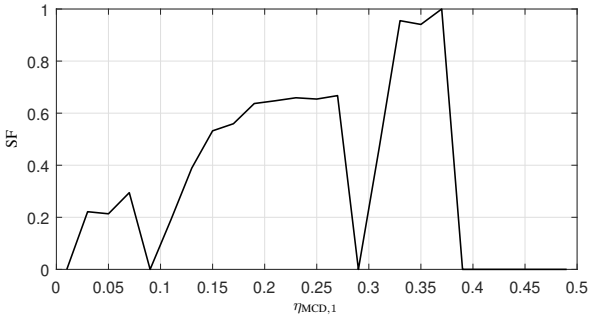

Fig. 5: SF variation versus $\eta_{\mathrm{MCD},1}$ variation at position 1.

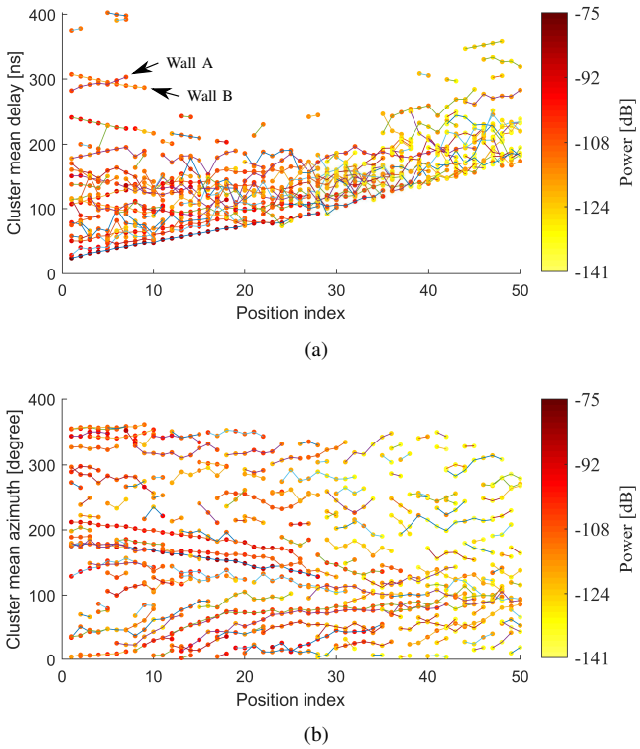

Fig. 6: Dynamic clusters identified and tracked. (a) Delay domain. (b) Azimuth domain.

Based on the obtained clustering results, cluster tracking are performed by checking MCDs among cluster centroids between neighboring positions as elaborated in Algorithm 2. For each old cluster identified at the kth position, the closest new cluster is determined by finding the cluster at the $(k+1)$th position with minimum MCD to this old cluster. The closest

Algorithm 1 The proposed MCD-threshold-based clustering algorithm for individual positions.

Input: MPC parameters $\mathbf{\Theta}^{(k)}$ at the kth array position.
Output: Clustering results $\mathcal{L}_c^{(k)}; c \in \mathcal{C}^{(k)}$.

1: Initialize path-index set $\mathcal{L} \leftarrow \{1, \ldots, L^{(k)}\}$
2: Initialize cluster index $i \leftarrow 0$
3: **while** $\mathcal{L} \neq \emptyset$ **do**
4: $i \leftarrow i + 1$
5: Find the index of the path with highest power $\ell_{\mathrm{m}} = \arg\max_{\ell \in \mathcal{L}} |\alpha_\ell^{(k)}|^2$
6: Initialize path-index set for the ith cluster $\mathcal{L}_i^{(k)} \leftarrow \emptyset$
7: **for** $\ell \in \mathcal{L}$ **do**
8: **if** $\mathrm{MCD}_{\ell,\ell_m} \leq \eta_{\mathrm{MCD},1}$ **then**
9: $\mathcal{L}_i^{(k)} \leftarrow \mathcal{L}_i^{(k)} + \{\ell\}$
10: **end if**
11: **end for**
12: $\mathcal{L} \leftarrow \mathcal{L} \setminus \mathcal{L}_i^{(k)}$
13: **end while**
14: Let cluster-index set $\mathcal{C}^{(k)} \leftarrow \{1, \ldots, i\}$
15: Calculate all the cluster centroids $\mu_c^{(k)}; c \in \mathcal{C}^{(k)}$ by (7)
16: **while** $\mu_c^{(k)}$'s do not keep unchanged **do**
17: Initialize $\mathcal{L} \leftarrow \{1, \ldots, L^{(k)}\}$ and $\mathcal{L}_c^{(k)} \leftarrow \emptyset; c \in \mathcal{C}^{(k)}$
18: **for** $\ell \in \mathcal{L}$ **do**
19: Find the centroid index c_n with minimum MCD to the current MPC: $c_n = \arg\min_{c \in \mathcal{C}^{(k)}} \mathrm{MCD}_{\ell, \mu_c^{(k)}}$
20: **if** $\mathrm{MCD}_{\ell, \mu_{c_n}^{(k)}} \leq \eta_{\mathrm{MCD},1}$ **then**
21: $\mathcal{L}_{c_n}^{(k)} \leftarrow \mathcal{L}_{c_n}^{(k)} + \{\ell\}$, $\mathcal{L} \leftarrow \mathcal{L} \setminus \{\ell\}$
22: **end if**
23: **end for**
24: **if** $\mathcal{L} \neq \emptyset$ **then**
25: $i \leftarrow i + 1$, **do** lines 3 to 12.
26: **end if**
27: Update $\mathcal{C}^{(k)}$ and $\mu_c^{(k)}; c \in \mathcal{C}^{(k)}$
28: **end while**

Algorithm 2 The proposed cluster tracking algorithm between neighboring positions.

Input: Clustering results at all positions.
Output: Cluster tracking results.

1: $i \leftarrow 1$
2: **for** $i \leq (K-1)$ **do**
3: Obtain cluster centroids $\mu_c^{(i)}; c \in \mathcal{C}^{(i)}$
4: Obtain cluster centroids $\mu_c^{(i+1)}; c \in \mathcal{C}^{(i+1)}$
5: **for** $a \in \mathcal{C}^{(i)}$ **do**
6: Find nearest cluster at the $(i+1)$th position: $b_n = \arg\min_{c \in C^{(i+1)}} \mathrm{MCD}_{\mu_a^{(i)}, \mu_c^{(i+1)}}$
7: Find nearest cluster back at the ith position: $a_n = \arg\min_{c \in C^{(i)}} \mathrm{MCD}_{\mu_c^{(i)}, \mu_{b_n}^{(i+1)}}$
8: **if** $a_n = a$, and $\mathrm{MCD}_{\mu_a^{(i)}, \mu_{b_n}^{(i+1)}} \leq \eta_{\mathrm{MCD},2}$ **then**
9: Associate clusters a^i and b_n^{i+1} as one cluster
10: **end if**
11: **end for**
12: Update cluster index set $\mathcal{C}^{(i+1)}$. The associated cluster-index values are set identical to previous values in $\mathcal{C}^{(i)}$, and un-associated cluster-index values accumulate referring to the largest value in $\mathcal{C}^{(i)}$.
13: $i \leftarrow i + 1$
14: **end for**

old cluster to each new cluster is determined vice versa. If an old cluster and a new cluster are mutually closest, and their MCD is lower than a pre-defined threshold $\eta_{\mathrm{MCD},2}$, these two clusters are associated as a tracked cluster. Old clusters that are not associated are considered "dead" clusters that stop existing, and new clusters that are not associated are considered as "born" clusters. In our case, $\eta_{\mathrm{MCD},2}$ is empirically chose as 0.35 to obtain reasonable tracking results.[5] Figs. 6(a) and 6(b) illustrate the cluster identification and tracking results in delay and azimuth domains, respectively. Each dot represents a cluster's centroid in delay or azimuth. The colors of dots denote clusters power, and the dots belong to one cluster are connected with lines. It can be observed that clusters evolve in delay and azimuth domains. For examples, it can be observed in Fig. 6(a) that the delay and azimuth of LoS cluster increases and decreases respectively along the route, and it stops at position 28 where the LoS link is starting to be blocked. Moreover, the clusters caused by "Wall A" and "Wall B" can also be easily located in Fig. 6. A clearer illustration of them is in Fig. 11. It can be observed that the cluster delays of them increases and decreases respectively, whereas the cluster azimuths almost keep unchanged as 180 and 360 (or 0) degrees, respectively. The demonstrated consistency between tracked clusters and the underlying propagation mechanisms validates the performance of the proposed cluster identification and tracking algorithm.

[5]The value of $\eta_{\mathrm{MCD},2}$ is selected practically. The attempt is to guarantee the cluster tracking results provide good match with the physical propagation mechanisms. In addition, it is noteworthy that the path-index set of tracked LoS cluster is associated as $\mathcal{L}_1^{(k)}$ in the algorithm since the power of the LoS cluster is the highest in the first array position.

V. Dynamic channel model

Based on the cluster identification and tracking results, a dynamic channel model is established for the hall and corridor scenarios in this section. Basically, three aspects of the channel characteristics have been investigated. *i)* The composite-level parameters that include path loss, composite root-mean-square (RMS) delay spreads, composite RMS azimuth spreads are presented in Sect. V-A. *ii)* In Sect. V-B, cluster-level parameters, i.e. cluster delay spread, cluster azimuth spread, cluster power decay and correlations thereof, are elaborated. *iii)* Sect. V-C describes the "birth-death" behaviours of clusters. The investigated parameters include cluster survival length, cluster birth location, cluster evolution and cluster number. Note that the statistics obtained in *i)* and *ii)* can be exploited to reproduce random/wide-sense-stationary (WSS) channel realizations according to procedures similar to that as specified in,

e.g. [53].[6] In cases where the spatial consistency (or dynamics) of the channel is crucial, statistics obtained in *iii)* can be further exploited to reproduce the realistic dynamic/non-WSS channels.

A. Composite level parameters

1) Path Loss PL: According to the clustering results, the received power at the kth position can be calculated as

$$p = \sum_{\ell \in \{\mathcal{L} \backslash \mathcal{L}_1\}} |\alpha_\ell|^2 \tag{9}$$

where $\mathcal{L} = \{1, \ldots, L^{(k)}\}$, and the superscript k is omitted in (9) for notation convenience. The LoS cluster is not included for the following reasons. *i)* The challenging communication scenario at mm-wave frequency bands is usually the case where LoS direction is blocked. By removing LoS cluster in hall, a fair comparison can be obtained between the hall and corridor scenarios with only NLoS clusters considered. *ii)* Compared to that of NLoS clusters, the behaviour of LoS cluster is rather deterministic which is investigated in Sect.V-B and can be easily included in the link budget estimation together with (9) if LoS communication is targeted. The floating-intercept (also known as alpha-beta) path loss model

$$PL(d)[\text{dB}] = \alpha + 10 \cdot \beta \log_{10}(d/d_0) + X_\sigma \tag{10}$$

is exploited, where α denotes the intercept, β indicates the path loss exponent (PLE), d and d_0 represent the Tx-to-Rx distance (the length of the straight line connecting the Tx and Rx positions) and reference distance (set as 1 m) respectively, and X_σ is the shadow fading modeled as a Gaussian random variable with zero mean and standard deviation σ. Fig. 7 illustrates the path loss fitting in both hall and corridor scenarios. It can be observed the PLE in hall is small as 0.96. This can be explained by the fact that the hall is a nearly-closed scenario, the power of NLoS clusters change insignificantly with the array moving. However, the PLE in corridor is high as 5.9, mostly due to the large attenuation caused by the multiple reflections from the sidewalls in the corridor.

2) Composite delay spread σ_τ and composite azimuth spread σ_ϕ: The RMS delay spread is the most common parameter to characterize the delay dispersion of the channel, which is calculated as the second-order central moment of the power delay profile. Specifically, by using the HRPE estimation results, the RMS delay spread can be calculated as specified in [55], [56]

$$\sigma_\tau = \sqrt{\overline{\tau^2} - \overline{\tau}^2} \tag{11}$$

[6]The term "random" here means that the channel parameters are generated independently for each snapshot according to the obtained statistics. In other words, the spatial consistency between neighboring channel snapshots are not considered. However, in 5G and beyond-5G communication systems where massive MIMO is considered as the key enabling technology, it is crucial to evaluated the beam-management [7], [54] (e.g. beam acquisition and beam tracking) performance of devices, which necessitates the investigation for aspect *iii)* in this contribution.

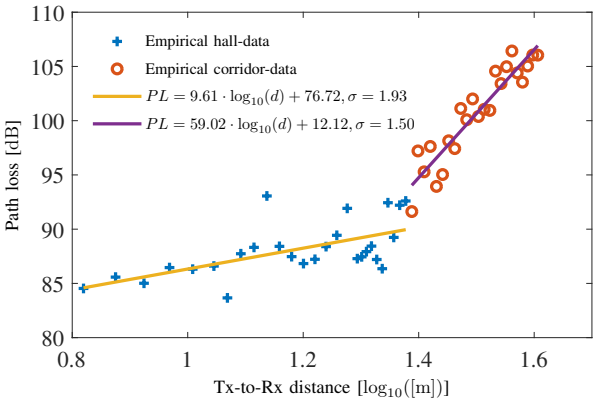

Fig. 7: Path loss fitting for the hall scenario and corridor scenario.

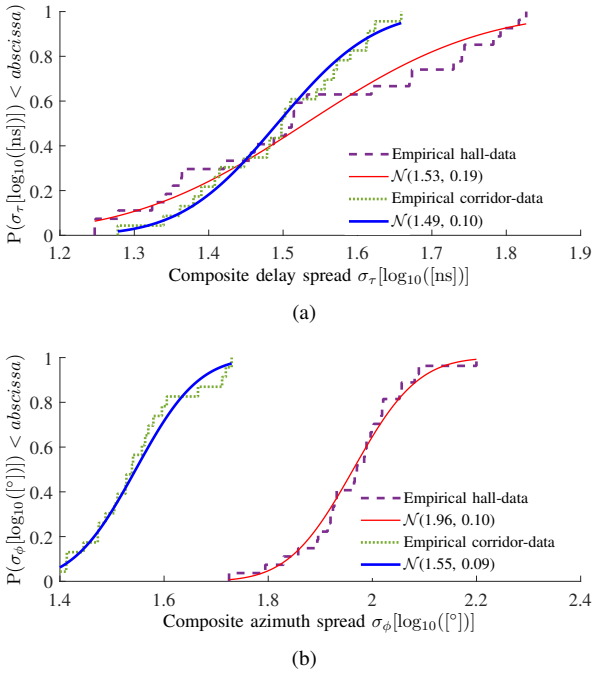

Fig. 8: Empirical and fitted analytical CDFs for hall and corridor scenarios. (a) Composite delay spread σ_τ. (b) Composite azimuth spread σ_ϕ.

with

$$\overline{\tau^2} = \frac{\sum_{\ell \in \{\mathcal{L} \backslash \mathcal{L}_1\}} |\alpha_\ell|^2 \cdot \tau_\ell^2}{\sum_{\ell \in \{\mathcal{L} \backslash \mathcal{L}_1\}} |\alpha_\ell|^2}, \quad \overline{\tau} = \frac{\sum_{\ell \in \{\mathcal{L} \backslash \mathcal{L}_1\}} |\alpha_\ell|^2 \cdot \tau_\ell}{\sum_{\ell \in \{\mathcal{L} \backslash \mathcal{L}_1\}} |\alpha_\ell|^2} \tag{12}$$

The azimuth spread σ_ϕ can be calculated as [53]

$$\sigma_\phi = \sqrt{-2\log\left(\left|\frac{\sum_{\ell \in \{\mathcal{L} \backslash \mathcal{L}_1\}} \exp(j\phi_\ell) \cdot |\alpha_\ell|^2}{\sum_{\ell \in \{\mathcal{L} \backslash \mathcal{L}_1\}} |\alpha_\ell|^2}\right|\right)} \tag{13}$$

Fig. 8(a) and Fig. 8(b) illustrate the empirical cumulative distribution functions (CDFs) of σ_τ and σ_ϕ represented in logarithm

scales respectively for both hall and corridor scenarios, and the empirical CDFs are well fitted with normal distributions.[7] It can be observed from Fig. 8(a) that in most cases, the composite delay spread in hall scenario is larger than that observed in corridor scenario. We postulate that this is mainly due to the fact that the dimension of the hall is large, and MPCs with larger relative delays can exist. Meanwhile, in some cases, the delay spread in hall can be smaller than that of corridor. This is possibly due to that the objects in the hall can cause dominant paths which compress the whole spread. Moreover, it can be observed from Fig. 8(b) that the composite azimuth spread in the hall is larger that that in the corridor. Basically, this is due to the large dimension of the hall, which implies that MPCs can have different azimuth angles. As a contrast, the corridor has a narrow opening to the hall, which leads to confined azimuth angles of the paths. Consequently, we can observe small composite azimuth spread in the corridor scenario.

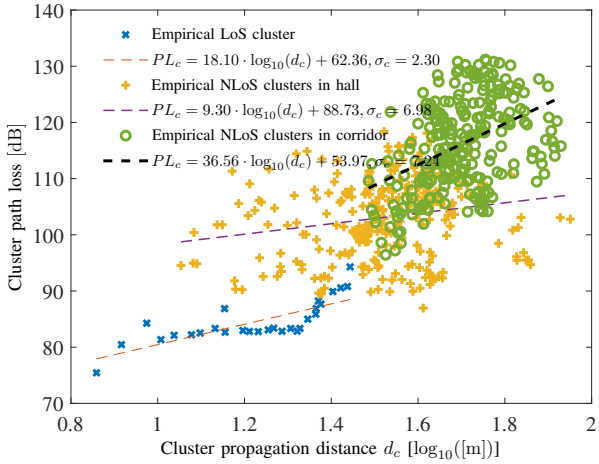

Fig. 9: Cluster power decay behaviour for LoS cluster and NLoS cluster in hall and corridor scenarios.

B. Cluster level parameters

1) Cluster power decay behaviour: The cluster power decay PL_c is similarly modeled using (9) with PL replaced by the cluster path loss PL_c and d replaced by d_c calculated according to the cluster mean delay $\bar{\tau}_c$. Fig. 9 illustrates the cluster path loss versus propagation distance in logarithmic scale for LoS cluster in hall, NLoS clusters in hall scenario and NLoS clusters in corridor scenario, respectively. It can be observed that PLE of LoS cluster is near to the free-space PLE 2, which is reasonable. It can also be observed that the PLE of NLoS clusters in corridor scenario is higher as 3.65. The possible reason is that the narrow corridor lead to larger reflection orders hence a larger PLE. However, as a contrast, the PLE of NLoS clusters in hall scenario is small. We postulate this is because the objects, e.g. the metal objects, in the hall can cause high-power clusters although with large propagation distances, which tilts down the slope. This also results in a large shadowing for the NLoS clusters in hall compared to that of LoS cluster. Basically, it can be observed that the spread of cluster path loss becomes larger with the cluster propagation distance increasing. We postulate it is due to the fact that with a larger propagation distance, the possibility of clusters experiencing multiple-bounces is higher. As different objects or scatterers can cause different losses, the path loss spread could thus be larger.

2) Intra-cluster delay spread σ_{τ_c} and azimuth spread σ_{ϕ_c}: The intra-cluster delay spread and azimuth spread are calculated similarly by using (11) and (13), respectively, with path index-set replaced by the corresponding cluster path-index set.

[7]We exploit the Kolmogorov-Smirnov (KS) testing [57] to validate the consistency between the empirical distribution and the fitted analytical distribution. Specifically, if the p-value is larger than a pre-defined significance level α, the null hypothesis is accepted, say, the empirical and fitted distributions are consistent. Note that the value selection of α is rather artificial (conventionally at 0.05 meaning the probability of wrongly rejecting the null hypothesis), we thus directly show p-values throughout the paper. For example in the case illustrated here, the p-values are 0.74 and 0.97 that are much larger than 0.05, which indicates that the consistency between the empirical and fitted distribution are rather significant. All the p-values for the fittings throughout the paper can be found in Table IV.

Fig. 10(a) and Fig. 10(b) illustrate respectively the empirical CDFs of σ_{τ_c} and σ_{ϕ_c} for the LoS cluster and NLoS clusters in hall and corridor, and the fitted analytical CDFs are also shown. It can be observed from Fig. 10(a) and Fig. 10(b) that both the delay spread and azimuth spread of LoS cluster are smaller than that of NLoS clusters. This is reasonable since the high power of LoS path compresses the cluster dispersion in both domains. Moreover, it can also be observed that the cluster delay spreads and azimuth spreads of NLoS clusters in hall are smaller than that observed in corridor scenario. We conjecture this is because in the hall, sparsely placed objects such as pillars can cause clusters with dominant MPC(s). However, in the corridor, due to the narrow dimension, MPCs with similar power are grouped as a cluster which enlarges the cluster dispersion.

3) Correlations of cluster level parameters: The correlation coefficient between two random variables X and Y is formulated as

$$\gamma_{XY} = \frac{\sum_i (X_i - \bar{X})(Y_i - \bar{Y})}{\sqrt{\sum_i (X_i - \bar{X})^2}\sqrt{\sum_i (Y_i - \bar{Y})^2}} \tag{14}$$

where $\bar{X}$ and $\bar{Y}$ represent the mean values of X and Y, respectively. Table III summarizes the correlation coefficients among cluster power, cluster delay spread and cluster azimuth spread. It can be observed that the correlation coefficients $\gamma(\sigma_{\tau_c}, p_c)$ and $\gamma(\sigma_{\phi_c}, p_c)$ of LoS cluster are negative and significant. This is reasonable since the power of LoS cluster is mainly dominated by the LoS path, and with a higher LoS path power, the LoS cluster dispersions in both delay and azimuth are compressed. For the same reason, a positive $\gamma(\sigma_{\tau_c}, \sigma_{\phi_c})$ for LoS cluster is also observed. The NLoS clusters exhibit similar correlation trends among these cluster-level parameters. However, the absolute values are rather small. Therefore, it can be considered that no correlations have been found among cluster-level parameters for NLoS cluster in both hall and corridor scenarios.

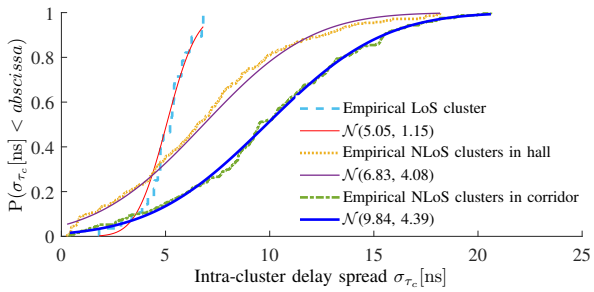

(a)

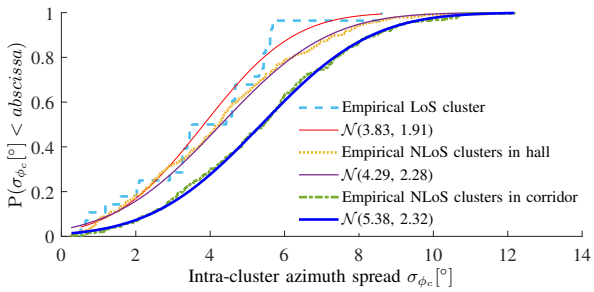

(b)

Fig. 10: Empirical and fitted CDFs of intra-cluster delay spread and azimuth spread for LoS cluster, hall and corridor scenarios. (a) Intra-cluster delay spread σ_{τ_c}. (b) Intra-cluster azimuth spread σ_{ϕ_c}.

Table III: Correlations among cluster level parameters.

	LoS	NLoS in hall	NLoS in corridor
$\gamma(\sigma_{\tau_c}, \sigma_{\phi_c})$	0.28	0.14	0.05
$\gamma(\sigma_{\tau_c}, p_c)$	-0.56	-0.08	-0.08
$\gamma(\sigma_{\phi_c}, p_c)$	-0.48	-0.15	-0.02

C. Dynamic parameters

In this section, dynamic parameters that characterize the "birth-death" behaviors of clusters are investigated. The concerned parameters include the cluster survival length, cluster born point, slopes of cluster-trajectories in both delay and azimuth domains. Fig. 11 illustrates two enlarged clusters selected from Fig. 6 to demonstrate the definitions of the dynamic parameters. Note that to compromise the model accuracy and complexity, we use linear lines to fit the cluster-trajectories in both delay and azimuth domains. This is a reasonable approximation since it can be observed from Fig. 6 and Fig. 11 that the cluster survival length is usually not large, which means that during the "alive" distance, the relative geometry between a cluster and the scatterer do not change much, thus a first-order approximation is reasonable. Specifically, the variation of a dynamic cluster in terms of mean delay and mean azimuth can be formatted as

$$\bar{\tau}_c = a_\tau d + b_\tau + x_\tau, \quad \bar{\phi}_c = a_\phi d + b_\phi + x_\phi \qquad (15)$$

where d denotes the distance the UCA moves along the route, and a, b and x represent the slope, intercept and fluctuation respectively with their subscripts τ and ϕ indicating delay and azimuth domains, respectively.

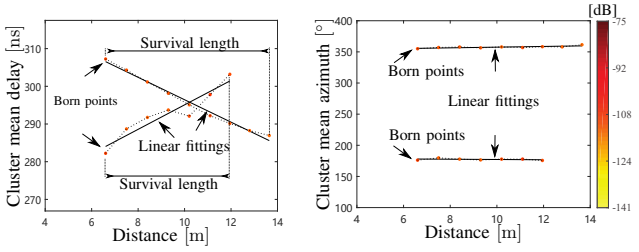

(a) (b)

Fig. 11: An example demonstration of dynamic parameters with two clusters enlarged from Fig. 6.

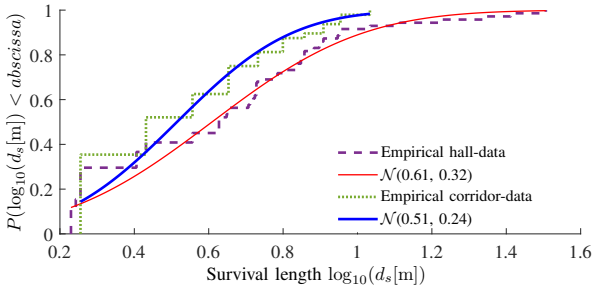

(a)

Fig. 12: Empirical and fitted CDFs of survival distance d_s in logarithm scale for NLoS clusters in hall and corridor.

1) Survival length d_s: Fig. 12 illustrates the empirical CDFs of cluster survival lengths in logarithm scale for both hall and corridor scenarios. It can be observed that the empirical CDFs of survival length in meter can be well fitted using log-normal distributions. This means that the survival length has moderate values with large probability. In other words, either the survival length is too small or too large, its probability becomes smaller. Moreover, it can also be observed that the cluster survival length in hall is larger than that observed in corridor scenario. This is consistent with the fact that the dimension of the hall is large which can result in large cluster survival lengths. Due to the multiple reflections in corridor, clusters cannot be alive for long distances.

2) Slopes a_τ and a_ϕ of clusters: By fitting the model as specified in (15), a_τ and a_ϕ are calculated for the NLoS clusters in both hall and corridor scenarios. Fig. 13(a) and Fig. 13(b) illustrate the empirical CDFs and fitted analytical CDFs for a_τ and a_ϕ respectively in both scenarios. It can be observed that the spread of the slopes in the corridor scenario is basically larger than that observed in the hall scenario. We postulate the main reason is that the scatterers are nearer to the transceiver in the corridor due to its smaller dimension. In addition, Fig. 14(a) and Fig. 14(b) illustrate respectively the empirical CDFs of x_τ and x_ϕ for both scenarios, which are found to be best fitted with stable distributions.[8] It can be observed that the mean values of x_τ and x_ϕ are near 0, which is expected in (15). Moreover, the fluctuations x_τ or x_ϕ are similar in both scenarios.

[8]Readers are referred to [58] for the definition of stable distribution.

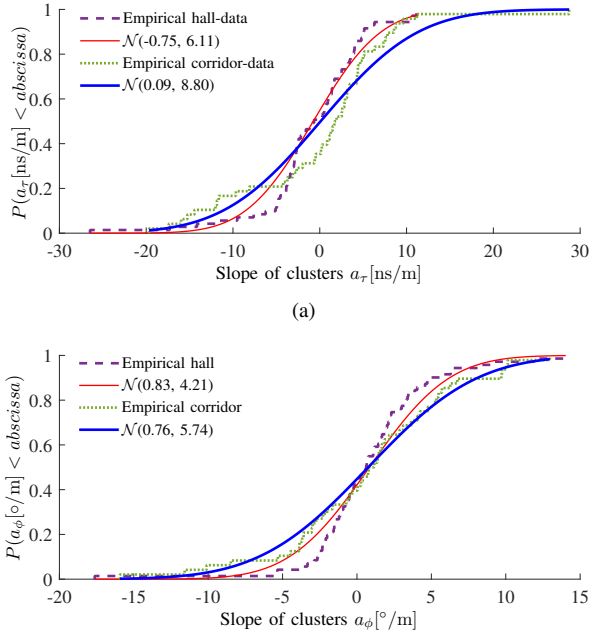

Fig. 13: Empirical and fitted CDFs of the slope for the NLoS clusters in hall and corridor scenarios. (a) Delay domain a_τ. (b) Azimuth domain a_ϕ.

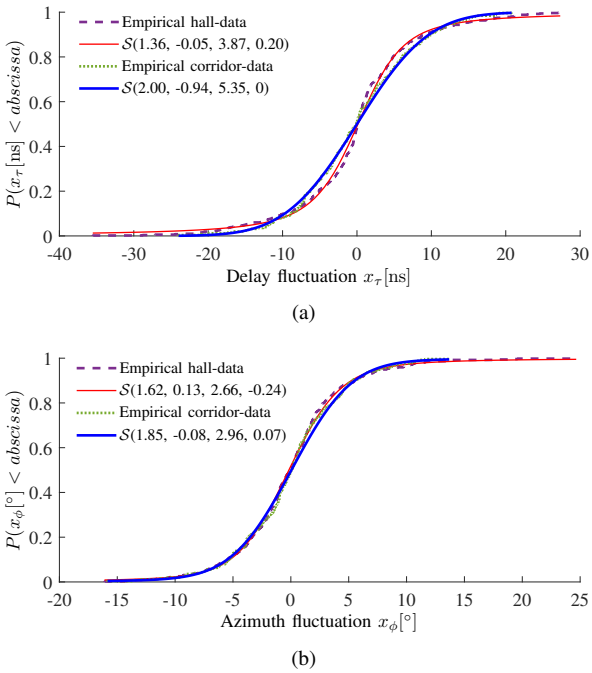

Fig. 14: Empirical and fitted CDFs of the delay and azimuth fluctuation for NLoS clusters in hall and corridor scenarios. (a) Delay fluctuation x_τ. (b) Azimuth fluctuation x_ϕ.

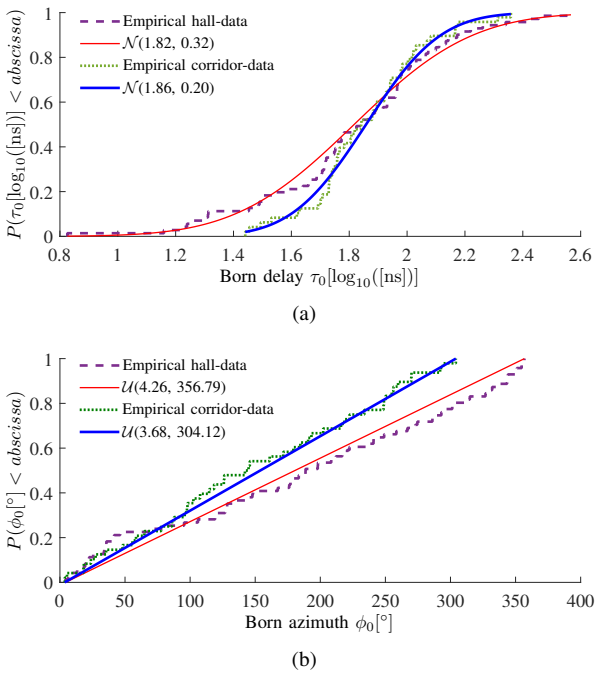

Fig. 15: Empirical and fitted CDFs of the born delay and born azimuth for NLoS clusters in hall and corridor scenarios. (a) Born delay τ_0. (b) Born azimuth ϕ_0.

3) Born delay τ_0 and born azimuth ϕ_0: As illustrated in Fig. 11, τ_0 and ϕ_0 of a cluster are defined as the delay (relative to LoS path delay) and azimuth of the cluster born point, respectively. Fig. 15(a) illustrates the empirical CDFs and fitted analytical CDFs for τ_0 in logarithmic scale in both scenarios. It can be observed that the range of τ_0 in hall scenario is larger than that observed in corridor. We postulate that this is due to the fact that the scatterer with large relative distance in hall can still cause non-negligible clusters. However, in the corridor scenario, larger relative delay probably means more bounces between two sidewalls, and the power of clusters decreases fast. Fig. 15(b) illustrates the empirical CDFs and the corresponding fitted CDFs for ϕ_0 in both scenarios. It can be observed that the empirical CDFs of born azimuth in both scenarios can be well fitted with uniform distributions. This is reasonable since the walls and objects as well as bounces in both scenarios can cause clusters with various angles. Besides, due to the dimension of the hall is larger, the whole angle range is larger than that observed in corridor.

4) Born clusters number N: Fig. 16 illustrates the empirical CDFs and the fitted CDFs of born clusters number for both scenarios. It can be observed that the mean number of born clusters in hall scenario is slightly larger than that observed in corridor, which we postulate is due to the larger dimension and more objects in hall scenario. However, the born clusters number are basically similar in both scenarios. The possible reason is that although the dimension of the corridor is smaller, with a glass wall on one side, the outside objects may also cause new-born clusters. It is noteworthy that if the cluster born-process can be considered as a Possion process, the mean value of N can be considered as the born rate of dynamic

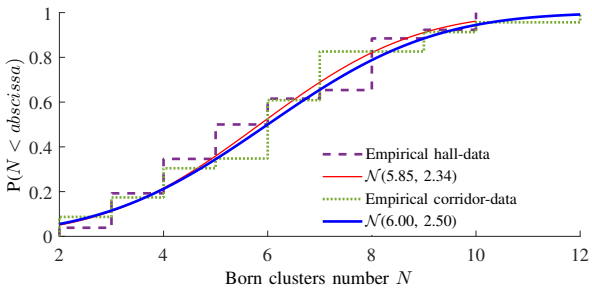

(a)

Fig. 16: Empirical and fitted CDFs of the born clusters number at each position for NLoS clusters in hall and corridor.

Table IV: Statistics extracted for the established dynamic model.

		Parmeters	Hall (Dist.; p-value)	Corridor (Dist.; p-value)
Composite level		$\sigma_\tau[\log_{10}([\text{ns}])]$	$\mathcal{N}(1.53, 0.19)$; 0.74	$\mathcal{N}(1.49, 0.10)$; 0.97
		$\sigma_\phi[\log_{10}([^\circ])]$	$\mathcal{N}(1.96, 0.10)$; 0.93	$\mathcal{N}(1.55, 0.09)$; 0.96
		$(\alpha, \beta, X_\sigma)$	(76.72, 0.96, 1.93)	(12.12, 5.90, 1.50)
Cluster level	LoS cluster	$\sigma_{\tau_c}[\text{ns}]$	$\mathcal{N}(5.05, 1.15)$; 0.77	-
		$\sigma_{\phi_c}[^\circ]$	$\mathcal{N}(3.83, 1.91)$; 0.68	-
		$(\alpha, \beta, X_\sigma)$	(62.36, 1.81, 2.30)	-
	NLoS clusters	$\sigma_{\tau_c}[\text{ns}]$	$\mathcal{N}(6.83, 4.08)$; 0.26	$\mathcal{N}(9.84, 4.39)$; 0.71
		$\sigma_{\phi_c}[^\circ]$	$\mathcal{N}(4.29, 2.28)$; 0.55	$\mathcal{N}(5.38, 2.32)$; 0.96
		$(\alpha, \beta, X_\sigma)$	(88.73, 0.93, 6.98)	(53.97, 3.66, 7.24)
Dynamic behavior		$d_s[\log_{10}([\text{m}])]$	$\mathcal{N}(0.61, 0.32)$; 0.04	$\mathcal{N}(0.51, 0.24)$; 0.02
		$a_\tau[\text{ns/m}]$	$\mathcal{N}$(-0.75, 6.11); 0.11	$\mathcal{N}(0.09, 8.80)$; 0.17
		$a_\phi[^\circ/\text{m}]$	$\mathcal{N}(0.83, 4.21)$; 0.25	$\mathcal{N}(0.76, 5.74)$; 0.85
		$x_\tau[\text{ns}]$	$\mathcal{S}$(1.36, -0.05, 3.87, 0.20); 0.11	$\mathcal{S}$(2.00, -0.94, 5.35, 0); 0.77
		$x_\phi[^\circ]$	$\mathcal{S}$(1.62, 0.13, 2.66, -0.24); 0.76	$\mathcal{S}$(1.85, -0.08, 2.96, 0.07); 0.59
		$\tau_0[\log_{10}([\text{ns}])]$	$\mathcal{N}(1.82, 0.32)$; 0.49	$\mathcal{N}(1.86, 0.20)$; 0.88
		$\phi_0[^\circ]$	$\mathcal{U}(4.26, 356.79)$; 0.37	$\mathcal{U}(3.68, 304.12)$; 0.95
		N	$\mathcal{N}(5.85, 2.34)$; 0.42	$\mathcal{N}(6.00, 2.50)$; 0.46

clusters. In addition, the statistics extracted for the established dynamic model are summarized in Table IV.

VI. Conclusions

In this contribution, a millimeter-wave channel measurement campaign at 28-30 GHz was conducted along a pre-defined 48 m route in an indoor area from a hall to a corridor. Based on the estimation results using a high resolution parameter estimation (HPRE) algorithm, a novel cluster identification and tracking algorithm was exploited to trace dynamic clusters observed in the channel. The composite-level, cluster-level and "birth-death" behaviours were investigated. It has been found that the composite path loss exponent (PLE) in the corridor can be high as 5.9, while its counterpart in the hall can be as small as 0.96, which is possibly due to the large attenuation caused by the multiple reflections in the corridor. The mean composite delay spread in the hall is slightly larger than that observed in the corridor, both of which are around 30 ns. Meanwhile, the mean composite azimuth spread in the hall was observed much larger than that observed in the corridor, which are around 91° and 35°, respectively. However, the cluster delay spread and cluster azimuth spread in the hall scenario are smaller than that observed in the corridor, mostly due to the fact that the objects in the hall can cause dominant paths. Moreover, cluster power decay behaviors are very different among the line-of-sight (LoS) cluster, non-LoS (NLoS) clusters in the hall and NLoS clusters in the corridor. The cluster survival length in both hall and corridor scenarios can be well fitted with log-normal distributions, and the mean survival lengths in hall and corridor were found as around 4.07 m and 3.24 m, respectively. The cluster born delay and born azimuth in both scenarios were found to obey log-normal and uniform distributions, respectively. In addition, it has been found that the born rate of clusters are similar in both scenarios. The overall statistics can be found in Table IV. The established dynamic model can provide valuable reference for evaluating the performance of 5G and beyond systems. Future works include further enhancing the model's ability by also including the dynamic behavious in the elevation domain, applying the proposed algorithm and analysis for outdoor propagation scenarios and adopting the developed dynamic cluster channel models for wireless system performance testing.

References

[1] M. Agiwal, A. Roy, and N. Saxena, "Next generation 5G wireless networks: A comprehensive survey," *IEEE Communications Surveys Tutorials*, vol. 18, no. 3, pp. 1617–1655, thirdquarter 2016.

[2] J. G. Andrews, S. Buzzi, W. Choi, S. V. Hanly, A. Lozano, A. C. K. Soong, and J. C. Zhang, "What will 5G be?" *IEEE Journal on Selected Areas in Communications*, vol. 32, no. 6, pp. 1065–1082, June 2014.

[3] C. Wang, F. Haider, X. Gao, X. You, Y. Yang, D. Yuan, H. M. Aggoune, H. Haas, S. Fletcher, and E. Hepsaydir, "Cellular architecture and key technologies for 5G wireless communication networks," *IEEE Communications Magazine*, vol. 52, no. 2, pp. 122–130, February 2014.

[4] A. Osseiran, F. Boccardi, V. Braun, K. Kusume, P. Marsch, M. Maternia, O. Queseth, M. Schellmann, H. Schotten, H. Taoka, H. Tullberg, M. A. Uusitalo, B. Timus, and M. Fallgren, "Scenarios for 5G mobile and wireless communications: the vision of the METIS project," *IEEE Communications Magazine*, vol. 52, no. 5, pp. 26–35, May 2014.

[5] W. Roh, J. Seol, J. Park, B. Lee, J. Lee, Y. Kim, J. Cho, K. Cheun, and F. Aryanfar, "Millimeter-wave beamforming as an enabling technology for 5G cellular communications: theoretical feasibility and prototype results," *IEEE Communications Magazine*, vol. 52, no. 2, pp. 106–113, February 2014.

[6] S. Sun, T. S. Rappaport, R. W. Heath, A. Nix, and S. Rangan, "MIMO for millimeter-wave wireless communications: beamforming, spatial multiplexing, or both?" *IEEE Communications Magazine*, vol. 52, no. 12, pp. 110–121, December 2014.

[7] M. Giordani, M. Polese, A. Roy, D. Castor, and M. Zorzi, "A tutorial on beam management for 3GPP NR at mmwave frequencies," *IEEE Communications Surveys and Tutorials*, 2019.

[8] L. Tian, V. Degli-Esposti, E. M. Vitucci, and X. Yin, "Semi-deterministic radio channel modeling based on graph theory and ray-tracing," *IEEE Transactions on Antennas and Propagation*, vol. 64, no. 6, pp. 2475–2486, June 2016.

[9] B. Ai, K. Guan, R. He, J. Li, G. Li, D. He, Z. Zhong, and K. M. S. Huq, "On indoor millimeter wave massive MIMO channels: Measurement and simulation," *IEEE Journal on Selected Areas in Communications*, vol. 35, no. 7, pp. 1678–1690, July 2017.

[10] D. He, B. Ai, M. Schmieder, Z. Zhong, J. Kim, B. Hui, H. Chung, I. Kim, and Y. Hao, "Influence analysis of typical objects in rural railway environments at 28 GHz," *IEEE Transactions on Vehicular Technology*, vol. 68, no. 3, pp. 2066–2076, March 2019.

[11] S. Hur, S. Baek, B. Kim, Y. Chang, A. F. Molisch, T. S. Rappaport, K. Haneda, and J. Park, "Proposal on millimeter-wave channel modeling for 5G cellular system," *IEEE Journal of Selected Topics in Signal Processing*, vol. 10, no. 3, pp. 454–469, April 2016.

[12] J. Chen, X. Yin, L. Tian, and M. Kim, "Millimeter-wave channel modeling based on a unified propagation graph theory," *IEEE Communications Letters*, vol. 21, no. 2, pp. 246–249, Feb 2017.

[13] T. S. Rappaport, G. R. MacCartney, M. K. Samimi, and S. Sun, "Wideband millimeter-wave propagation measurements and channel models for future wireless communication system design," *IEEE Transactions on Communications*, vol. 63, no. 9, pp. 3029–3056, Sep. 2015.

[14] G. R. Maccartney, T. S. Rappaport, M. K. Samimi, and S. Sun, "Millimeter-wave omnidirectional path loss data for small cell 5G channel modeling," *IEEE Access*, vol. 3, pp. 1573–1580, 2015.

[15] G. R. Maccartney, T. S. Rappaport, S. Sun, and S. Deng, "Indoor office wideband millimeter-wave propagation measurements and channel models at 28 and 73 GHz for ultra-dense 5G wireless networks," *IEEE Access*, vol. 3, pp. 2388–2424, 2015.

[16] C. Zhang, X. Yin, X. Cai, and Z. Yu, "Wideband 39 GHz millimeter-wave channel measurements under diversified vegetation," in *2018 IEEE 29th Annual International Symposium on Personal, Indoor and Mobile Radio Communications (PIMRC)*, Sep. 2018, pp. 1–6.

[17] C. Gustafson, K. Haneda, S. Wyne, and F. Tufvesson, "On mm-wave multipath clustering and channel modeling," *IEEE Transactions on Antennas and Propagation*, vol. 62, no. 3, pp. 1445–1455, March 2014.

[18] C. Ling, X. Yin, R. Möller, S. Häfner, D. Dupleich, C. Schneider, J. Luo, H. Yan, and R. Thomä, "Double-directional dual-polarimetric cluster-based characterization of 70-77 GHz indoor channels," *IEEE Transactions on Antennas and Propagation*, vol. 66, no. 2, pp. 857–870, Feb 2018.

[19] C. Ling, X. Yin, H. Wang, and R. S. Thomä, "Experimental characterization and multipath cluster modeling for 13-17 GHz indoor propagation channels," *IEEE Transactions on Antennas and Propagation*, vol. 65, no. 12, pp. 6549–6561, Dec 2017.

[20] J. Blumenstein, A. Prokes, A. Chandra, T. Mikulasek, R. Marsalek, T. Zemen, and C. Mecklenbräuker, "In-vehicle channel measurement, characterization, and spatial consistency comparison of 3-11 GHz and 55-65 GHz frequency bands," *IEEE Transactions on Vehicular Technology*, vol. 66, no. 5, pp. 3526–3537, May 2017.

[21] J. Huang, C. Wang, R. Feng, J. Sun, W. Zhang, and Y. Yang, "Multi-frequency mmwave massive MIMO channel measurements and characterization for 5G wireless communication systems," *IEEE Journal on Selected Areas in Communications*, vol. 35, no. 7, pp. 1591–1605, July 2017.

[22] J. Li, B. Ai, R. He, M. Yang, and Z. Zhong, "On modeling of dense multipath component for indoor massive MIMO channels," *IEEE Antennas and Wireless Propagation Letters*, vol. 18, no. 3, pp. 526–530, March 2019.

[23] F. Zhang and W. Fan, "Near-field ultra-wideband mmwave channel characterization using successive cancellation beamspace UCA algorithm," *IEEE Transactions on Vehicular Technology*, vol. 68, no. 8, pp. 7248–7259, Aug 2019.

[24] S. Sangodoyin, V. Kristem, A. F. Molisch, R. He, F. Tufvesson, and H. M. Behairy, "Statistical modeling of ultrawideband MIMO propagation channel in a warehouse environment," *IEEE Transactions on Antennas and Propagation*, vol. 64, no. 9, pp. 4049–4063, Sep. 2016.

[25] J. Chen, X. Yin, X. Cai, and S. Wang, "Measurement-based massive MIMO channel modeling for outdoor LoS and NLoS environments," *IEEE Access*, vol. 5, pp. 2126–2140, 2017.

[26] J. O. Nielsen, W. Fan, P. C. F. Eggers, and G. F. Pedersen, "A channel sounder for massive MIMO and mmwave channels," *IEEE Communications Magazine*, vol. 56, no. 12, pp. 67–73, December 2018.

[27] S. Malkowsky, J. Vieira, L. Liu, P. Harris, K. Nieman, N. Kundargi, I. C. Wong, F. Tufvesson, V. Öwall, and O. Edfors, "The world's first real-time testbed for massive MIMO: Design, implementation, and validation," *IEEE Access*, vol. 5, pp. 9073–9088, 2017.

[28] P. Harris, S. Malkowsky, J. Vieira, E. Bengtsson, F. Tufvesson, W. B. Hasan, L. Liu, M. Beach, S. Armour, and O. Edfors, "Performance characterization of a real-time massive MIMO system with LOS mobile channels," *IEEE Journal on Selected Areas in Communications*, vol. 35, no. 6, pp. 1244–1253, June 2017.

[29] L. Pometcu and R. D'Errico, "Large scale and clusters characteristics in indoor sub-THz channels," in *IEEE 29th Annual International Symposium on Personal, Indoor and Mobile Radio Communications (PIMRC)*, Sep. 2018, pp. 1405–1409.

[30] E. M. Vitucci, F. Yu, L. Possenti, M. Zoli, F. Fuschini, M. Barbiroli, V. Degli-Esposti, K. Guan, and T. Kürner, "A study on dual-directional mm-wave indoor channel characteristics," in *European Conference on Antennas and Propagation (EuCAP)*, March 2019, pp. 1–5.

[31] X. Cai and W. Fan, "A complexity-efficient high resolution propagation parameter estimation algorithm for ultra-wideband large-scale uniform circular array," *IEEE Transactions on Communications*, vol. 67, no. 8, pp. 5862–5874, Aug 2019.

[32] A. W. Mbugua, W. Fan, K. Olesen, X. Cai, and G. F. Pedersen, "Phase-compensated optical fiber-based ultrawideband channel sounder," *IEEE Transactions on Microwave Theory and Techniques*, vol. 68, no. 2, pp. 636–647, 2020.

[33] W. Fan, A. W. Mbugua, X. Cai, and K. Olesen, "Development and experimental validation of an ultra-wideband channel sounder," in *13th European Conference on Antennas and Propagation (EuCAP)*, March 2019, pp. 1–5.

[34] "A-INFO-SZ-2003000/P Datasheet," Tech. Rep. [Online]. Available: http://www.ainfoinc.com/en/pro_pdf/new_products/antenna/Bi-Conical%20Antenna/tr_SZ-2003000-P.pdf

[35] S. S. Zhekov, A. Tatomirescu, and G. F. Pedersen, "Antenna for ultra-wideband channel sounding," *IEEE Antennas and Wireless Propagation Letters*, vol. 16, pp. 692–695, 2017.

[36] H. Krim and M. Viberg, "Two decades of array signal processing research: the parametric approach," *IEEE Signal Processing Magazine*, vol. 13, no. 4, pp. 67–94, Jul 1996.

[37] C. A. Balanis, *Antenna theory: analysis and design*. 3rd ed. Hoboken, NJ, USA: Wiley, 2005.

[38] Y. Ji, W. Fan, and G. F. Pedersen, "Channel characterization for wide-band large-scale antenna systems based on a low-complexity maximum likelihood estimator," *IEEE Transactions on Wireless Communications*, vol. 17, no. 9, pp. 6018–6028, Sep. 2018.

[39] B. H. Fleury, M. Tschudin, R. Heddergott, D. Dahlhaus, and K. I. Pedersen, "Channel parameter estimation in mobile radio environments using the SAGE algorithm," *IEEE Journal on Selected Areas in Communications*, vol. 17, no. 3, pp. 434–450, Mar 1999.

[40] T. Moon, "The expectation-maximization algorithm," *IEEE Signal Processing Magazine*, 1997.

[41] M. Feder and E. Weinstein, "Parameter estimation of superimposed signals using the EM algorithm," *IEEE Transactions on Acoustics, Speech, and Signal Processing*, vol. 36, no. 4, pp. 477–489, April 1988.

[42] F. Zhang, W. Fan, and G. F. Pedersen, "Frequency-invariant uniform circular array for wideband mm-wave channel characterization," *IEEE Antennas and Wireless Propagation Letters*, vol. 16, pp. 641–644, 2017.

[43] X. Cai, W. Fan, X. Yin, and G. F. Pedersen, "Trajectory-aided maximum-likelihood algorithm for channel parameter estimation in ultra-wideband large-scale arrays," *IEEE Transactions on Antennas and Propagation*, pp. 1–1, 2020.

[44] N. Czink, R. Tian, S. Wyne, F. Tufvesson, J. Nuutinen, J. Ylitalo, E. Bonek, and A. F. Molisch, "Tracking time-variant cluster parameters in mimo channel measurements," in *the second International Conference on Communications and Networking in China*, Aug 2007, pp. 1147–1151.

[45] J. F. Trevor Hastie, Robert Tibshirani, *The Elements of Statistical Learning: Data Mining, Inference, and Prediction, Second Edition (Springer Series in Statistics)*, 2nd ed., ser. Springer Series in Statistics. Springer, 2009.

[46] R. He, Q. Li, B. Ai, Y. L. Geng, A. F. Molisch, V. Kristem, Z. Zhong, and J. Yu, "A kernel-power-density-based algorithm for channel multipath components clustering," *IEEE Transactions on Wireless Communications*, vol. 16, no. 11, pp. 7138–7151, Nov 2017.

[47] S. Cheng, M. Martinez-Ingles, D. P. Gaillot, J. Molina-Garcia-Pardo, M. Liénard, and P. Degauque, "Performance of a novel automatic identification algorithm for the clustering of radio channel parameters," *IEEE Access*, vol. 3, pp. 2252–2259, 2015.

[48] M. Steinbauer, H. Ozcelik, H. Hofstetter, C. F. Mecklenbrauker, and E. Bonek, "How to quantify multipath separation," *IEICE Transactions on Electronics*, vol. E85-C, no. 3, pp. 552–557, Mar 2002.

[49] N. Czink, P. Cera, J. Salo, E. Bonek, J. . Nuutinen, and J. Ylitalo, "Improving clustering performance using multipath component distance," *Electronics Letters*, vol. 42, no. 1, pp. 33–45, Jan 2006.

[50] U. Maulik and S. Bandyopadhyay, "Performance evaluation of some clustering algorithms and validity indices," *IEEE Transactions on Pattern Analysis and Machine Intelligence*, vol. 24, no. 12, pp. 1650–1654, Dec 2002.

[51] K. Kryszczuk and P. Hurley, "Estimation of the number of clusters using multiple clustering validity indices," in *Multiple Classifier Systems*, N. El Gayar, J. Kittler, and F. Roli, Eds. Berlin, Heidelberg: Springer Berlin Heidelberg, 2010, pp. 114–123.

[52] M. K. Pakhira, S. Bandyopadhyay, and U. Maulik, "Validity index for crisp and fuzzy clusters," *Pattern Recognition*, vol. 37, no. 3, pp. 487 – 501, 2004.

[53] "Study on channel model for frequencies from 0.5 to 100 GHz," Tech. Rep., 3GPP TR 38.901 V15.0.0, Jun. 2018.

[54] P. Kyösti, L. Hentilä, J. Kyröläinen, F. Zhang, W. Fan, and M. Latva-Aho, "Emulating dynamic radio channels for radiated testing of massive MIMO devices," in *IET Conference Publications*, 2018.

[55] X. Cai, J. Rodríguez-Piñeiro, X. Yin, N. Wang, B. Ai, G. F. Pedersen, and A. P. Yuste, "An empirical air-to-ground channel model based on passive measurements in LTE," *IEEE Transactions on Vehicular Technology*, vol. 68, no. 2, pp. 1140–1154, Feb 2019.

[56] X. Cai, B. Peng, X. Yin, and A. P. Yuste, "Hough-transform-based cluster identification and modeling for V2V channels based on measurements," *IEEE Transactions on Vehicular Technology*, vol. 67, no. 5, pp. 3838–3852, May 2018.

[57] F. J. Massey, "The kolmogorov-smirnov test for goodness of fit," *Journal of the American Statistical Association*, vol. 46, no. 253, 1951.

[58] J. P. Nolan, "Numerical calculation of stable densities and distribution functions," *Communications in statistics. Stochastic models*, vol. 13, no. 4, pp. 759–774, 1997.

Xuesong Cai received the B.S. degree and the Ph.D. degree (Hons.) from Tongji University, Shanghai, China, in 2013 and 2018, respectively. In 2015, he conducted a three-month internship with Huawei Technologies, Shanghai, China. He was also a Visiting Scholar with Universidad Politécnica de Madrid, Madrid, Spain in 2016. From 2018-2020, he was a postdoctoral research fellow with the APMS section, Department of Electronic Systems, Aalborg University (AAU), Aalborg, Denmark. Since April 2020, he has been a postdoctoral fellow with the Wireless Communication Networks Section, Department of Electronic Systems, AAU, cooperating with Nokia Bell Labs. His research interests include propagation channel measurement, high-resolution parameter estimation, channel characterization, channel modeling, over-the-air testing and UAV communications for 5G wireless communications.

Dr. Cai was a recipient of the Chinese National Scholarship for Ph.D. Candidates and Excellent Student award in 2016, the Excellent Student award and the "ZTE Fantastic Algorithm" award in 2017, the Outstanding Doctorate Graduate awarded by Shanghai Municipal Education Commission and "ZTE Blue Sword-Future Leaders Plan" in 2018, and the "Seal of Excellence" with the European Horizon 2020's Marie Skłodowska-Curie actions call in 2019.

Guojin Zhang received her Bachelor degree in Information Engineering from China University of Mining and Technology, China in 2013, and a Master degree from China University of Petroleum (East China), China in 2016. From July 2016 to January 2018, she was with Ericsson Communications, China as a Network Engineer. She is currently working toward the Ph.D. degree at the Antennas, Propagation and Millimeter-wave Systems (APMS) Section with Aalborg University, Denmark. The focus of her work is on channel parameter estimation and radio propagation channel modeling in millimeter wave frequency bands.

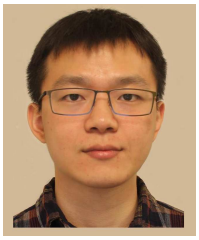

Chao Zhang received the B.S. and M.S. degrees in electronics science and technology from Tongji University, Shanghai, China, in 2013 and 2019, respectively. He is currently pursuing the doctoral degree in broadband communication with the Department of Electrical and Information Technology, Lund University, Sweden. His current research interests include channel modeling, array signal processing, Internet of Things, cloud computing and virtualization technology.

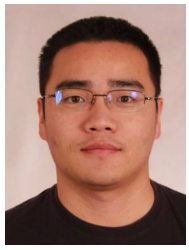

Wei Fan received his Bachelor of Engineering degree from Harbin Institute of technology, China in 2009, Master's double degree with highest honours from Politecnico di Torino, Italy and Grenoble Institute of Technology, France in 2011, and Ph.D. degree from Aalborg University, Denmark in 2014. From February 2011 to August 2011, he was with Intel Mobile Communications, Denmark as a research intern. He conducted a three-month internship at Anite telecoms oy (now Keysight technologies), Finland in 2014. His main areas of research are over-the-air testing of multiple antenna systems, radio channel sounding, modeling and emulation, and antenna array signal processing. He is currently an associate professor at the Antennas, Propagation and Millimeter-wave Systems (APMS) Section at Aalborg University.

Jinxing Li received the B.S. degree in communication engineering and Ph.D. degree in communication and information systems from Beijing Jiaotong University, Beijing, China, in 2011 and 2017, respectively. He is now a senior engineer in Huawei Technologies Co., Ltd., Shanghai. His research interests focus on MIMO OTA performance evaluation and standardization of user equipment.

Gert Frølund Pedersen was born in 1965. He received the B.Sc. and E.E. (Hons.) degrees in electrical engineering from the College of Technology in Dublin, Dublin Institute of Technology, Dublin, Ireland, in 1991, and the M.Sc.E.E. and Ph.D. degrees from Aalborg University, Aalborg, Denmark, in 1993 and 2003, respectively. Since 1993, he has been with Aalborg University where he is a Full Professor heading the Antennas, Propagation and Millimeter-wave Systems LAB with 25 researchers. He is also the Head of the Doctoral School on wireless communication with some 40 Ph.D. students enrolled. His research interests include radio communication for mobile terminals especially small antennas, diversity systems, propagation, and biological effects. He has published more than 500 peer reviewed papers, 6 books, 12 book chapters and holds over 50 patents. He has also worked as a Consultant for developments of more than 100 antennas for mobile terminals including the first internal antenna for mobile phones in 1994 with lowest SAR, first internal triple-band antenna in 1998 with low SAR and high TRP and TIS, and lately various multiantenna systems rated as the most efficient on the market. He has worked most of the time with joint university and industry projects and have received more than 21 M$ in direct research funding. He is currently the Project Leader of the RANGE project with a total budget of over 8 M$ investigating high performance centimetre/millimetre-wave antennas for 5G mobile phones. He has been one of the pioneers in establishing over-the-air measurement systems. The measurement technique is now well established for mobile terminals with single antennas and he was chairing the various COST groups with liaison to 3GPP and CTIA for over-the-air test of MIMO terminals. He is currently involved in MIMO OTA measurement.